

The Causes of Peripheral Coronal Loop Contraction and Disappearance Revealed in a Magnetohydrodynamic Simulation of Solar Eruption

JUNTAO WANG,^{1,2} CHAOWEI JIANG,¹ DING YUAN,¹ AND PENG ZOU¹

¹*Institute of Space Science and Applied Technology, Harbin Institute of Technology, Shenzhen 518055, People's Republic of China*

²*Nanchang Institute of Technology, Nanchang 330044, People's Republic of China*

ABSTRACT

The phenomenon of peripheral coronal loop contraction during solar flares and eruptions, recently discovered in observations, gradually intrigues solar physicists. However, its underlying physical mechanism is still uncertain. One is Hudson (2000)'s implosion conjecture which attributes it to magnetic pressure reduction in the magnetic energy liberation core, while other researchers proposed alternative explanations. In previous observational studies we also note the disappearance of peripheral shrinking loops in the late phase, of which there is a lack of investigation and interpretation. In this paper, we exploit a full MHD simulation of solar eruption to study the causes of the two phenomena. It is found that the loop motion in the periphery is well correlated with magnetic energy accumulation and dissipation in the core, and the loop shrinkage is caused by a more significant reduction in magnetic pressure gradient force than in magnetic tension force, consistent with the implosion conjecture. The peripheral contracting loops in the late phase act as inflow to reconnect with central erupting structures, which destroys their identities and naturally explains their disappearance. We also propose a positive feedback between the peripheral magnetic reconnection and the central eruption.

Keywords: Sun: corona; Sun: flares; magnetohydrodynamics (MHD)

1. INTRODUCTION

Solar flares and eruptions are the most violent activities releasing enormous energy in the solar system. The liberated energy, in the form of radiation, plasma thermal and non-thermal energy, and bulk kinetic energy, is believed to originate from free magnetic energy stored in coronal nonpotential magnetic field. Because of the equivalence between magnetic energy density and pressure, solar events could cause a significant reduction in magnetic pressure in the energy releasing core. Based on this argument, Hudson (2000) conjectured a phenomenon termed coronal implosion, which predicts that the plasma and entrained magnetic field would collapse into the region of reduced magnetic pressure, and coronal loop contraction may be one of manifestations.

Aly (1984, 1991) and Sturrock (1991) demonstrated that for simply connected force-free field with a given magnetic flux distribution at the bottom boundary, the open-field configuration in which all the field lines are opened to infinity possesses the maximum energy. It implies that closed field could not completely open through ideal MHD pro-

cesses spontaneously without extra energy input. However, in observations filament eruptions without flares are prevalent (e.g., Zou et al. 2019). To resolve this contradiction, Sturrock et al. (2001) proposed a metastable flux rope model in 3D where the flux rope is anchored below a restraining arcade and can erupt with the overlying field partially open. Following MHD simulations which exploited this magnetic configuration of Sturrock et al. (2001) showed that during the eruption, part of the unopened arcade field straddling the two legs of the flux rope would finally shrink toward the erupting core (Aulanier et al. 2005; Gibson & Fan 2006; Fan & Gibson 2007; Rachmeler et al. 2009).

Though the theoretical argument and simulations both support the existence of the phenomenon of coronal loop contraction in solar energy releasing events, its observational evidence is rare so far, compared to massive samples of solar eruptions and flares. Contractions of coronal loops with a face-on geometry were observed at the periphery of active regions in extreme ultraviolet in a few events (Liu & Wang 2009; Gosain 2012; Liu et al. 2012; Sun et al. 2012; Simões et al. 2013; Yan et al. 2013; Kushwaha et al. 2015; Wang et al. 2016). It was in doubt that these apparent loop contractions may just be a projection effect as accompanied eruptions could push peripheral loops to incline. Then Petrie (2016) and Wang et al. (2018) reported edge-on coronal loop con-

tractions, directly substantiating the reality of the contracting motion. Especially, Wang et al. (2018) showed in two events that without significant eruptions, loops could still shrink toward flaring regions. Simões et al. (2013) found a good correlation between loop contraction speed and radiation in hard X-ray and microwave.

In some events, considerable oscillations of the contracting loops (or part of the contracting loops) were also observed (Liu & Wang 2010; Gosain 2012; Liu et al. 2012; Sun et al. 2012; Simões et al. 2013). Liu & Wang (2010) suggested that magnetic strands with different contracting speeds may interact to produce oscillations. Russell et al. (2015) proposed a model where one loop is regarded as a harmonic oscillator with its equilibrium position changing due to underlying magnetic energy release, trying to provide a unified interpretation of loop contractions and oscillations. Sarkar et al. (2017) implemented the first MHD simulation concentrating on implosion, which found that loops in regions of different plasma β may exhibit different dynamic properties, and both kink and sausage modes of oscillations could exist when loops contract. Pascoe et al. (2017) took loop shrinkage into account in coronal seismology analysis, and only found the fundamental kink mode for the event in Simões et al. (2013).

Although the implosion phenomenon was conjectured by Hudson (2000) as due to magnetic pressure reduction in magnetic energy liberation region, Zuccarello et al. (2017) and Dudík et al. (2017) proposed alternative physical explanations for the peripheral coronal loop contraction. They attributed the contracting motion of the loops around the periphery to the return part of a vortex flow. However, in order to study the change in loop motion, either from a static state to contraction or from expansion to contraction, the acting forces should be analysed. Thus in terms of forces, Zuccarello et al. (2017) eliminated magnetic pressure or energy reduction below the contracting loops as a candidate, which results in the only possibility of enhanced magnetic tension in a zero- β MHD simulation. Especially, in Sections 3.2.2 and 3.2.3 of Zuccarello et al. (2017), “generates magnetic tension” or “magnetic tension increases” was frequently invoked. Though “overpressure” was also used in Section 3.2.3 of Zuccarello et al. (2017), their Figure 9 shows that the magnetic pressure gradient is outward rather than inward, which thus could not explain the loop contraction. They also exploited an analogy between the hydrodynamic and MHD cases for vortex generation, but the underlying forces in these two situations are very different. In hydrodynamic case, the fluid pressure is predominant, and the vortex generation is related to viscosity, while in coronal MHD the Lorentz force or its two components, i.e., magnetic tension force and magnetic pressure gradient force, dominate, and viscosity can be neglected in the simulation. Therefore, the underlying physics for peripheral coronal loop contraction is still contro-

versial. In addition, we note a phenomenon of disappearance of shrinking loops (or part of shrinking loops) in previous studies (Liu & Wang 2009; Sun et al. 2012; Simões et al. 2013; Yan et al. 2013; Kushwaha et al. 2015; Petrie 2016; Wang et al. 2016, 2018), which has not been investigated and interpreted so far.

In this paper, we will utilize an MHD simulation to both qualitatively and quantitatively study the dynamics of peripheral contracting loops, trying to reveal the physical mechanisms of their motion and disappearance. The MHD model is described in Section 2, and the analysis of peripheral contracting loops is detailed in Section 3. Discussion and conclusions are presented in Section 4.

2. METHOD

The MHD model is aimed to simulate the energy accumulation and initiation of solar eruption in a simple bipolar active region through a self-consistent way, which is similar to some previous studies (e.g., Amari et al. 2003; Aulanier et al. 2010). We solve the isothermal MHD equations as follows with non-dimensionalization on an adaptively refining mesh in 3D Cartesian geometry using an advanced conservation element and solution element (CESE) method (Jiang et al. 2010).

$$\frac{\partial \rho}{\partial t} + \nabla \cdot (\rho \mathbf{v}) = 0 \quad (1)$$

$$\rho \frac{D\mathbf{v}}{Dt} = -\nabla p + \mathbf{J} \times \mathbf{B} + \rho \mathbf{g} + \nabla \cdot (\nu \rho \nabla \mathbf{v}) \quad (2)$$

$$\frac{\partial \mathbf{B}}{\partial t} = \nabla \times (\mathbf{v} \times \mathbf{B}), \quad (3)$$

where ρ is the mass density, \mathbf{v} the plasma velocity, p the plasma thermal pressure, \mathbf{J} the electric current density, \mathbf{g} the gravitational acceleration, and \mathbf{B} the magnetic field. A small kinetic viscosity ν in the momentum Equation (2) is used for the purpose of keeping numerical stability during the very dynamic phase of the simulation. The coefficient $\nu = 0.05 \Delta x^2 / \Delta t$ corresponds to a grid Reynolds number of 10 for the length of a grid cell Δx . Though the resistivity is set as zero within the simulation volume, magnetic reconnection can occur via numerical diffusion when the thickness of a current layer approaches the grid size. The material derivative $D\mathbf{v}/Dt$ in the momentum Equation (2) represents the time rate of change in the velocity of a certain plasma element, as it flows along its streamline. The computational box is $(-24, -24, 0) < (x, y, z) < (24, 24, 48)$, sufficiently large to minimize numerical influences by side and top boundaries. The volume is resolved by a nonuniform block-structured grid with the highest and lowest resolution $\Delta x = \Delta y = \Delta z = 1/16$ and $1/4$, separately. The parameters for non-dimensionalization related in this paper are $L_s = 16$ arcsec = 11.52 Mm, $t_s = 52.5$ s, $v_s = 110$ km s⁻¹, $\rho_s = 2.29 \times 10^{-15}$ g cm⁻³ and $B_s = 1.86$ G for the length,

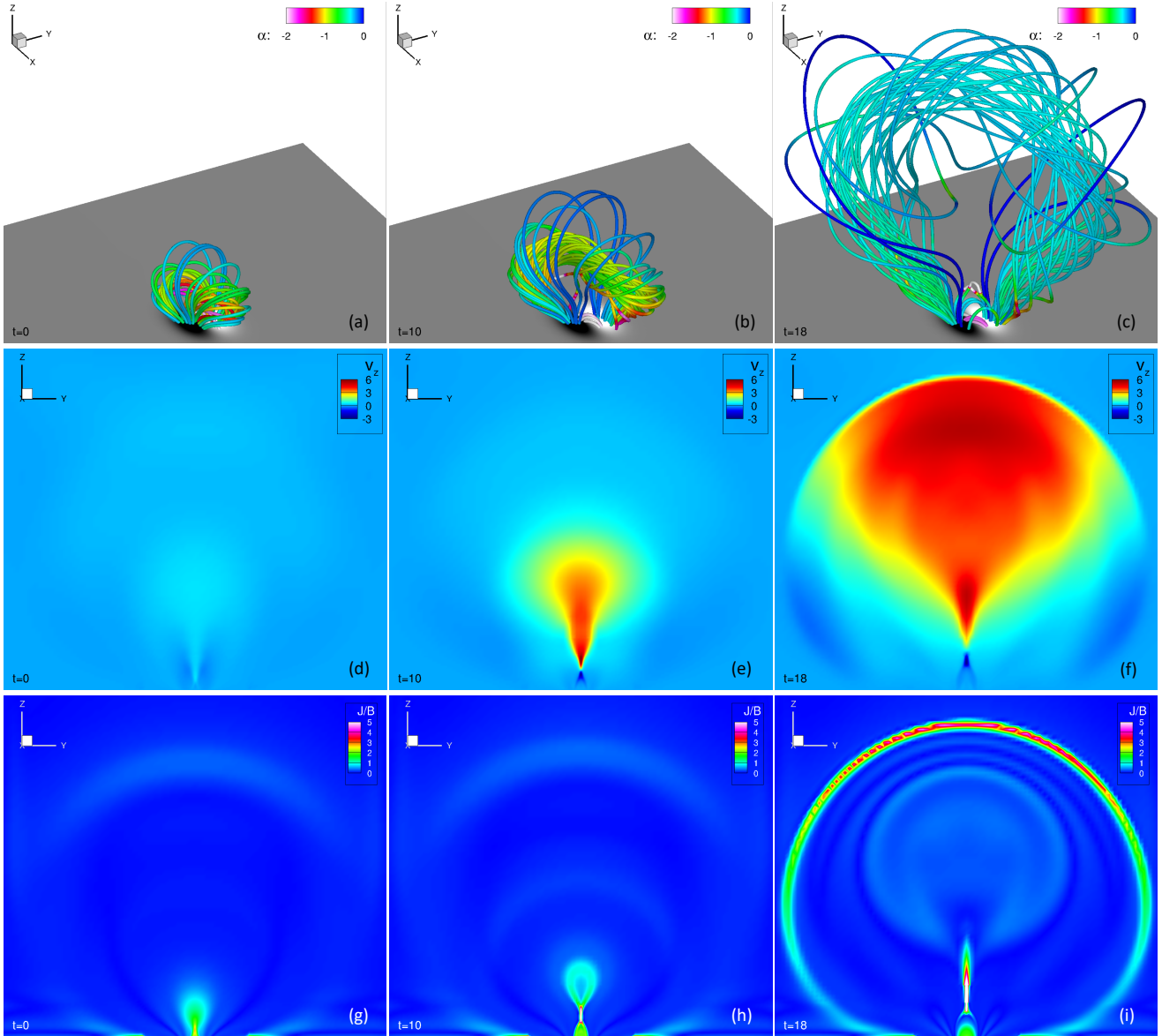


Figure 1. The eruption process in the simulation. (a)-(c) the evolution of magnetic field lines colored by the force-free parameter $\alpha = \mathbf{J} \cdot \mathbf{B} / B^2$. (d)-(f) vertical velocity evolution in the $x = 0$ plane. (g)-(i) current density evolution in the $x = 0$ plane.

time, velocity, density and magnetic field strength scales, respectively.

The initial conditions of the model are as follows. The magnetic field is potential with a bottom boundary similar to the one in [Amari et al. \(2003\)](#), mimicking a bipole solar active region with a relatively strong field gradient near the polarity inversion line (PIL). The atmospheric plasma is stratified by gravity with no flow, and the temperature is uniform. To ensure plasma $\beta < 1$ in the lower corona with a minimum value of 5×10^{-3} , the local gravitational coefficient is defined to decrease with increasing height.

The complete simulation comprises four phases in sequence. We first quasi-statically energize the initial potential magnetic field through two vortex flows centred on each po-

larity at the bottom boundary, which mimics sunspot rotation during flux emergence and creates sheared arcade field. Then it is switched to a relaxation phase without boundary driving. After that, surface diffusion possessing an enhanced photospheric resistivity is applied to simulate magnetic flux cancellation observed in the decay phase of active regions ([Aulanier et al. 2010](#)). Finally, when the system becomes unstable and the field eruption commences, any driving is ceased on the photophore which holds the magnetic field line-tied. The simulation continues until any disturbance from the eruption reaches any of the side and top boundaries. Further details of the model settings, the full evolution of the four stages, as well as the triggering mechanism and magnetic topology evolution during the eruption are to be described elsewhere

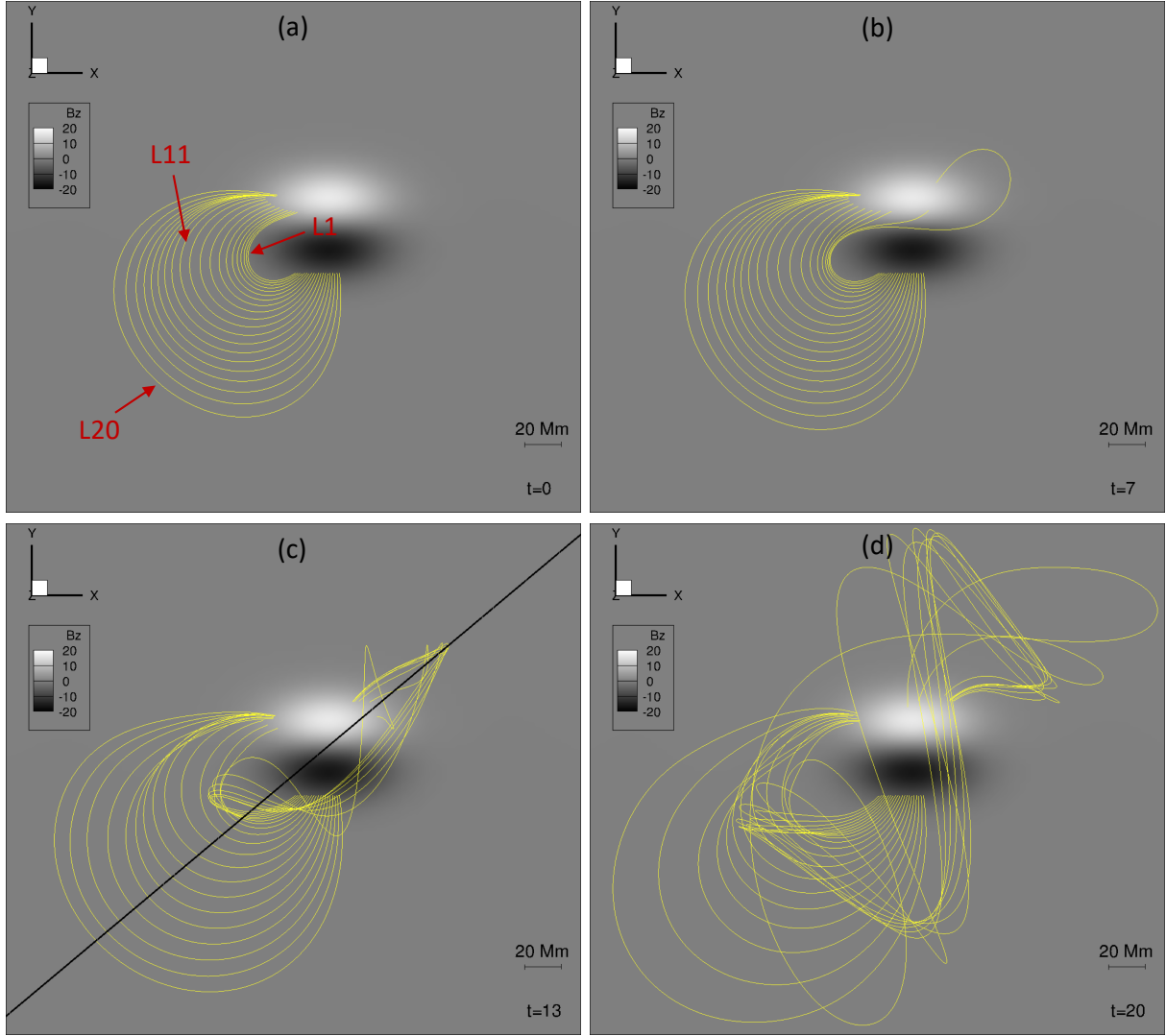


Figure 2. The positions and motion of selected peripheral magnetic loops at a face-on state from a top view perspective in the MHD simulation. The animated version of this figure is available, which runs from $t = 0$ to $t = 20$.

(Jiang et al. 2021, in preparation). In this study, we only focus on the last phase when the magnetic field erupts outwards and, in particular, the motions of the peripheral magnetic loops associated with the eruption.

3. RESULTS

3.1. Peripheral Magnetic Loop Motion

Figure 1 illustrates the evolution of erupting magnetic field lines, the vertical velocity and current density in the $x = 0$ plane, i.e., the central cross section of the computational volume in the simulation, which shows a thin current sheet connecting an erupting plasmoid and a cusp structure of post flare loops below, a typical process of a coronal mass ejection in observations (e.g., Sun et al. 2015; Wang et al. 2016) and many previous numerical simulations with different scenarios (e.g., Linker et al. 2003; Fan 2010; Török et al. 2018). In order to study the peripheral loop dynamics, we select 20

magnetic loops traced from the negative polarity to study, as shown in Figures 2 with a face-on view. These loops, possessing minor shear, are anchored at the periphery of the active region with relatively low magnetic strength compared with the central area. From $t = 0$ to $t = 20$, they behave dynamically when the eruption happens at the center; and different loops experience different physical processes, which we discuss in detail in Figure 3. As we can see from the associated animation attached, all of these peripheral loops eventually contract apparently towards the central polarities. In Figures 4 and the associated animations, with an edge-on perspective, the loop contraction instead of just inclination is evident. From Figures 2(a) and (b), we note that the peripheral contracting loops reside in a second inflow area ($V_{\text{slice}} > 0$, where V_{slice} represents the velocity in the chosen slice in Figure 2(c), and red color indicates direction towards right, blue towards left), separated from the traditional inflow

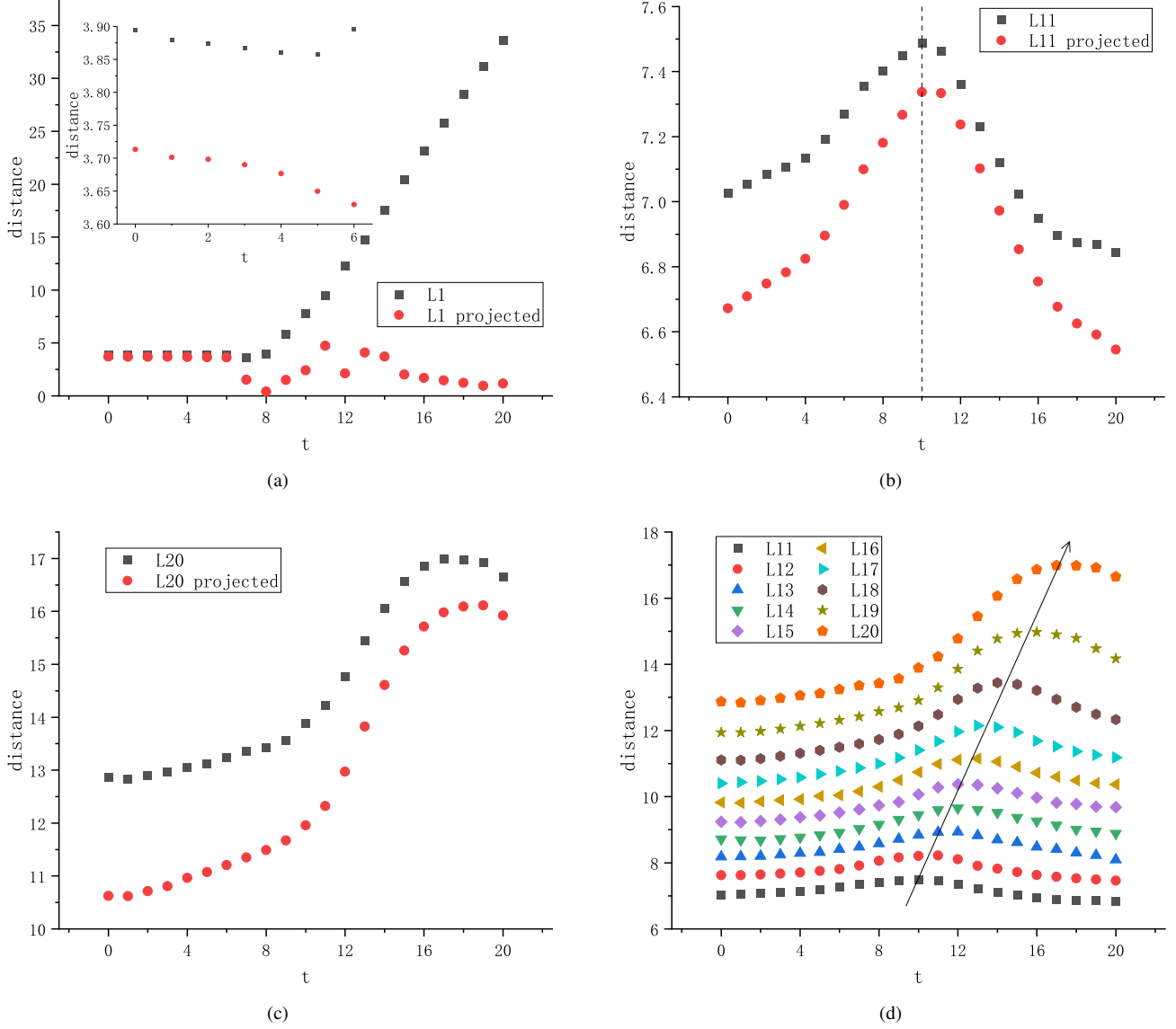


Figure 3. The detailed kinetics of selected peripheral magnetic loops. (a) for the innermost loop L1. The plot is enlarged for the data from $t = 0$ to $t = 6$ in the inset. (b) for the middle loop L11. The dashed line shows the transition from expansion to contraction. (c) for the outermost loop L20. (d) for L11 through L20. The arrow roughly links the inflection points from expansion to contraction for these loops.

region in the center. Figures 4(c) and (d) also show that the shrinking loops and the second inflow area are located between two thin layers of high current density, with the outer one corresponding to the shock produced by the eruption, and the inner one related to reconnection between the contracting and erupting structures, which is discussed in Section 3.3.

In Figure 3(a), (b) and (c), we select 3 representative magnetic loops from Figure 2(a), that is, the innermost loop notated by “L1”, the 11th loop in the middle “L11”, and the outermost loop “L20”, respectively, to investigate their detailed kinetics. The black dots in these three figures represent the distance between the midpoint of the loop and the origin (the center at the bottom boundary) in the numerical box,

while the projected value of this distance from a top view (i.e., the perspective in Figures 2(a)-(d)) is denoted by the red ones. Combined with Figures 2(a)-(b) and the associated animation, Figure 3(a) and its inset show that L1 experiences running slipping towards the center from $t = 0$ to $t = 6$, then reconnects forming a sigmoid, and finally erupts away. Figure 3(b) presents that before $t = 10$, L11 undergoes two expansion phases, with the later one possessing a relatively higher speed, after which it begins to contract towards the center, and then at around $t = 15$ the contraction starts to decelerate. Both the real and projected distances at $t = 20$ is smaller than the ones at the beginning time $t = 0$, demonstrating a net contraction for L11, which is consistent with

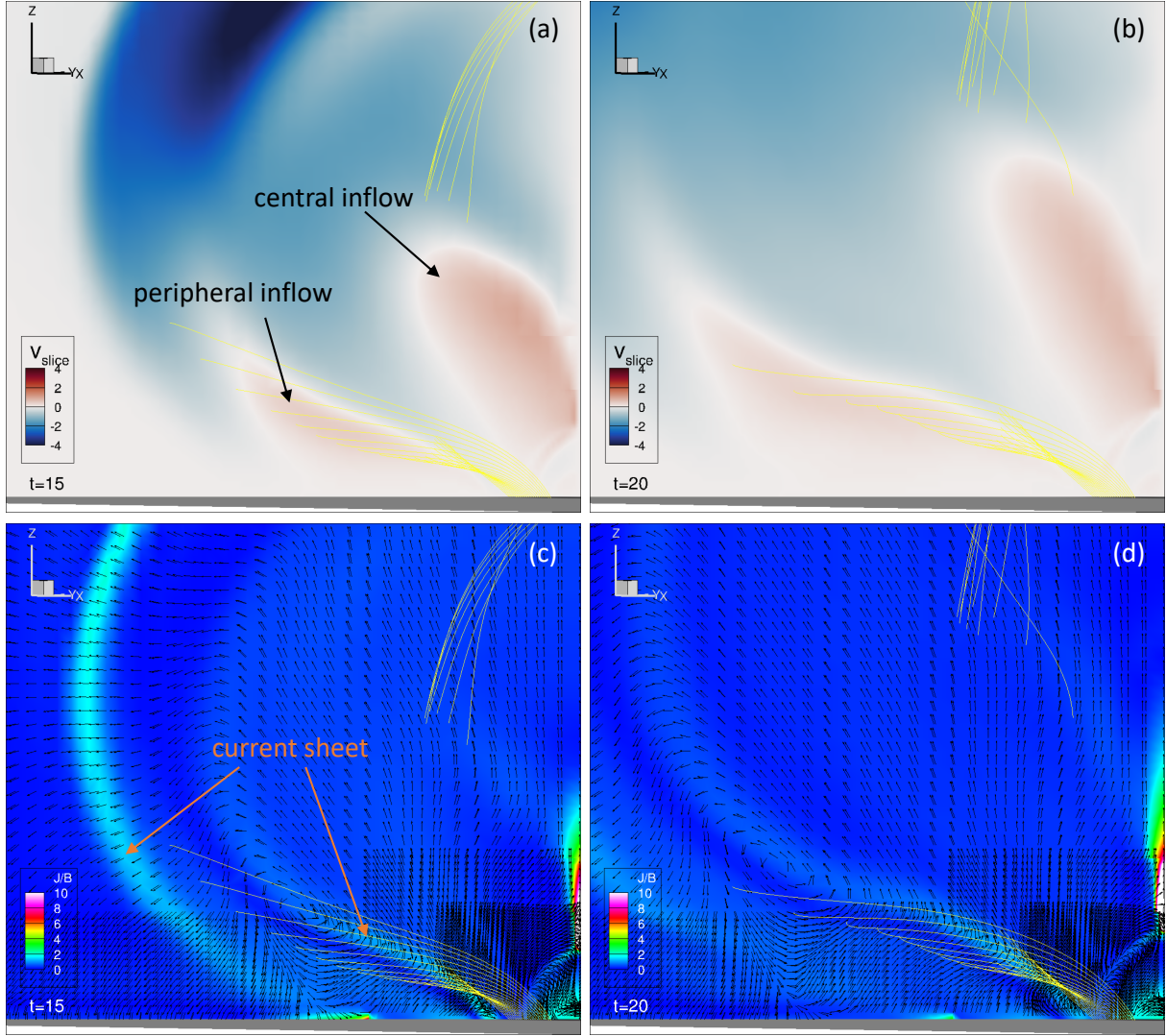


Figure 4. The selected peripheral magnetic loops at an edge-on state. The background slices are chosen to be the diagonal plane normal to $z = 0$ whose edge is indicated in Figure 2(c), with (a)-(b) colored by horizontal velocity in the slices, and (c)-(d) weighted current density. The arrows in (c)-(d) shows the velocity vectors in the chosen slices. The animated version of this figure is available, which runs from $t = 0$ to $t = 20$.

the observation in Wang et al. (2016). The motion of L20 is shown in Figure 3(c), which exhibits a similar behavior as L11 but without a full contraction phase due to the termination of the simulation. We expect that the contraction would proceed if the simulation continued. It is also noted that the transition from expansion to contraction for L20 is smoother than that for L11.

Figure 3(d) shows the distances between the midpoints of loops and the origin for L11 through L20 which do not experience reconnection during the period of the simulation. The arrow roughly links the inflection points from expansion to contraction for these magnetic loops, whose slope indicates an approximate speed 290 km s^{-1} with dimension for the outward propagating contraction signal, comparable to the

fast mode speed around the midpoints of the loops, thus consistent with the prediction in Wang et al. (2018).

3.2. Cause of Peripheral Magnetic Loop Contraction

In Figures 5(a)-(d) we plot the magnetic energy density $E_B = B^2/2 = 3.5$ isosurface colored with normalized current density J/B , to graphically investigate if the contraction of the selected magnetic loop is qualitatively correlated with magnetic energy release underneath proposed by Hudson (2000). Figures 5(e)-(h) show the corresponding magnetic energy density profile in the selected slice as in Figure 2(c). From $t = 0$ (Figure 5(a)) to $t = 8$ (Figure 5(b)), the selected isosurface experiences a slight inflation in the middle portion (the same as the evolution of the green profile from Figure 5(e) to Figure 5(f)), possibly due to magnetic energy

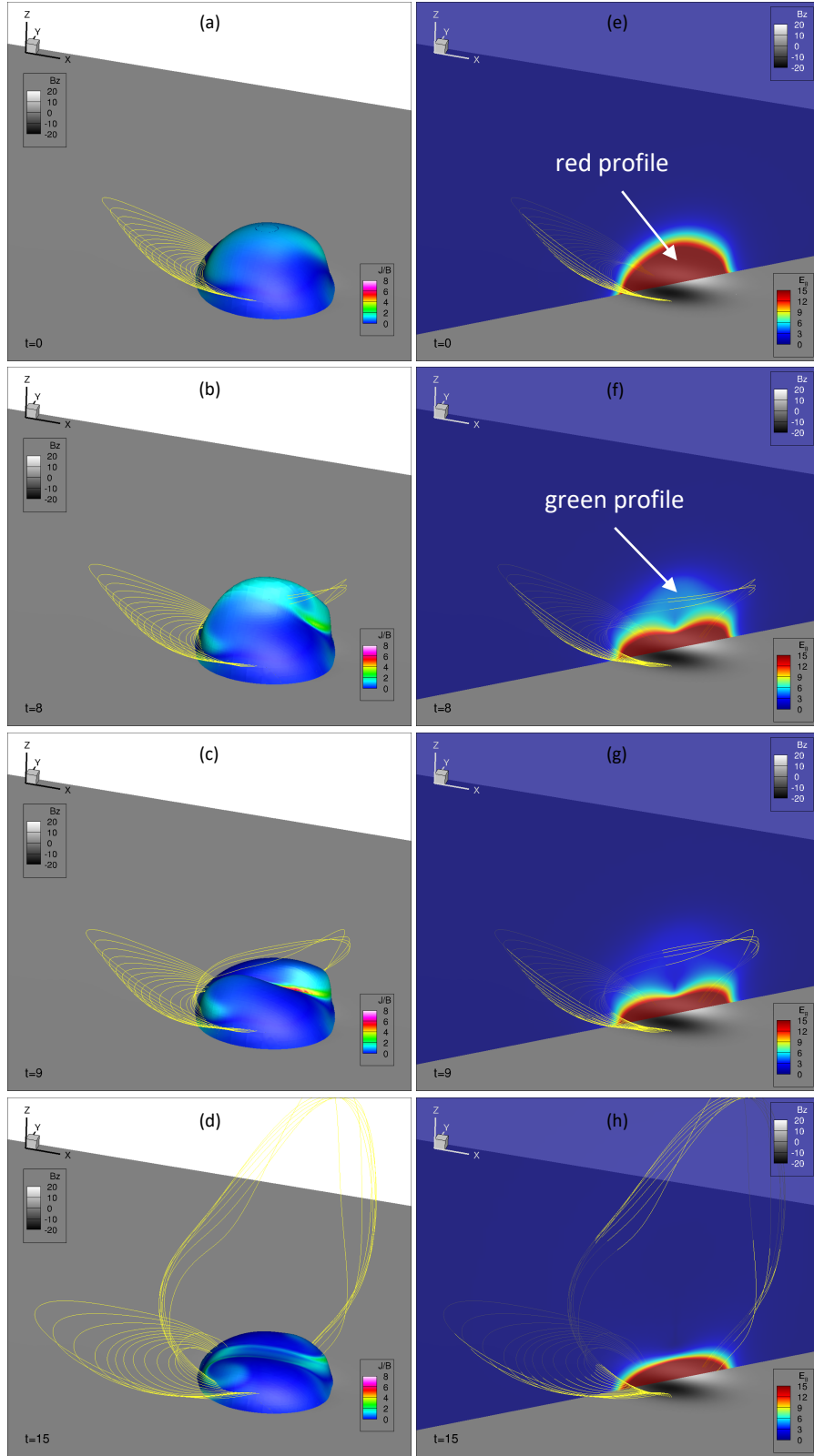


Figure 5. The correlation between peripheral magnetic loop motion and central magnetic energy. The isosurface in (a)-(d) denotes the magnetic energy density profile $E_B = 3.5$, colored with weighted current density. (e)-(h) indicates the corresponding magnetic energy density profile in the chosen slice as in Figure 2(c). The animated version of this figure is available, which runs from $t = 0$ to $t = 20$.

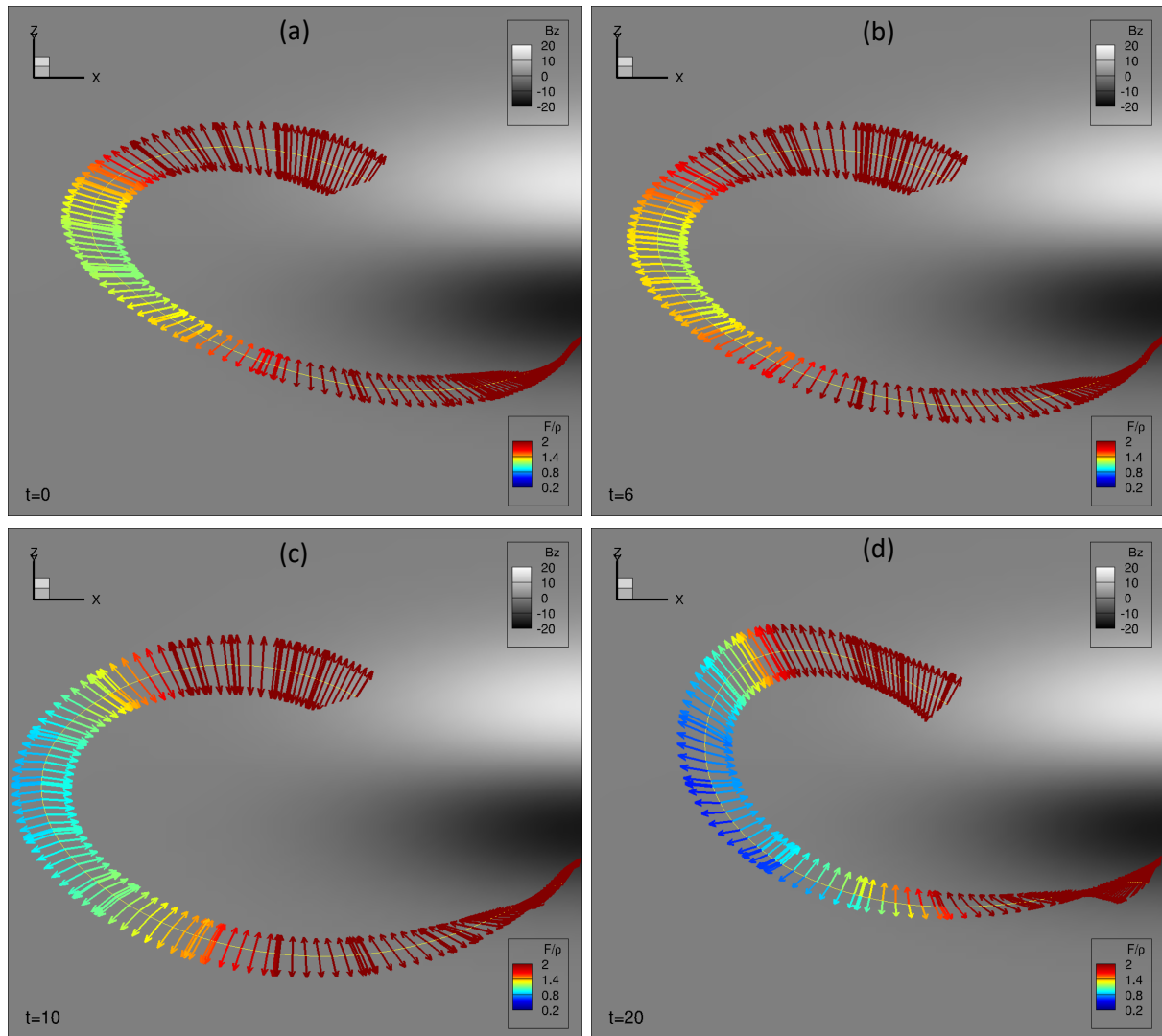


Figure 6. The correlation between peripheral magnetic loop motion and Lorentz force components. Outward and inward arrows represent MPN and MTN, colored by their magnitudes, respectively. The animated version of the figure is available, which runs from $t = 0$ to $t = 20$.

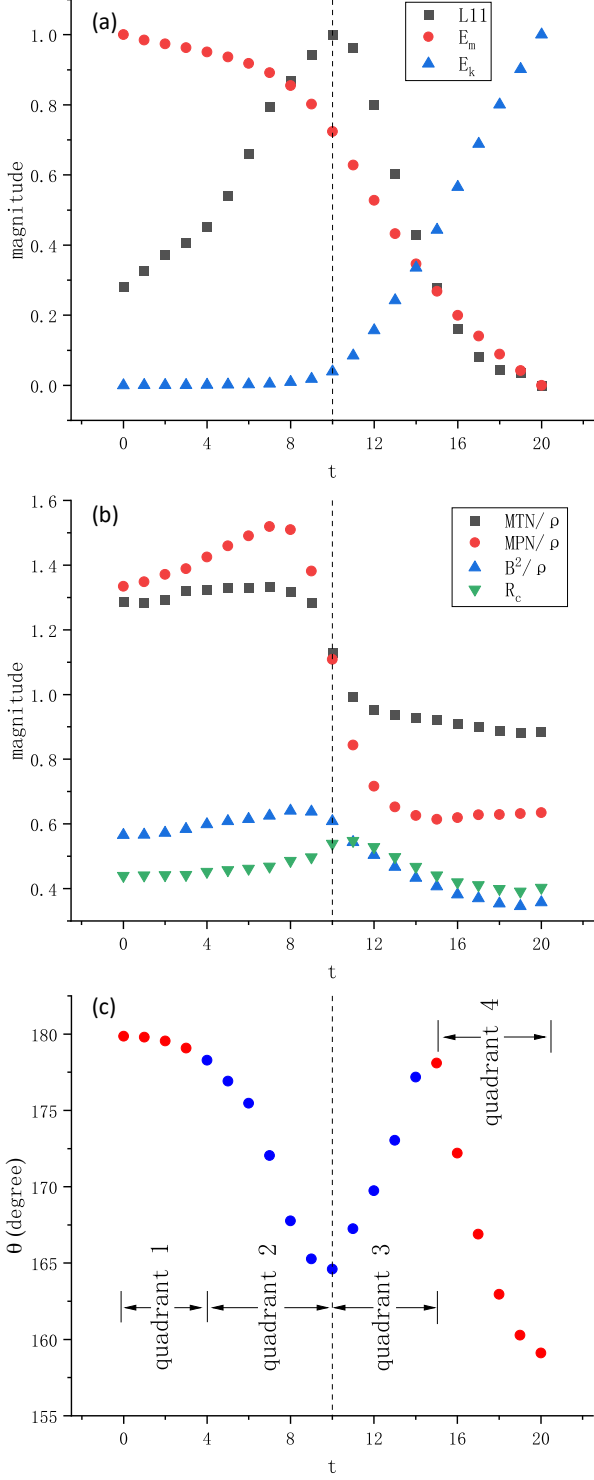


Figure 7. The dynamics of the magnetic loop L11. (a) the evolutions of normalized values of L11 distance as in Figure 3(b), magnetic energy E_m and plasma kinetic energy E_k in the simulation volume. (b) the changes in the magnitudes of MTN, MPN, B^2 (the three quantities are all weighted by the mass density ρ), and R_c with time. (c) the change in the angle between MTN and MPN with time. The dashed line shows the transition from expansion to contraction. The dashed line indicates the transition from expansion to contraction for L11.

accumulation as a result of gradual inflows from either side of the central tether-cutting reconnection (whose position can be viewed later in Figure 8(d)) in the preflare phase. During this period, the peripheral loops experience pre-eruption slow expansion except that the inner ones have reconnection which may cause the enhanced current in the inflating middle portion of the isosurface. Though the red profile descends possibly caused by the gradual central tether-cutting reconnection dissipation, the global magnetic structure does not erupt, which can be seen from the attached animation and also from the plasma kinetic energy later in Figure 7(a). At around $t = 9$ (Figure 5(c)) the isosurface suddenly collapses downward (corresponding to the collapse of the green profile in Figure 5(g)), which could be caused by a runaway dissipation of magnetic energy in the central reconnection just beneath the reconnected inner peripheral loops. The accelerated dissipation of magnetic energy at around $t = 9$ can be clearly seen later in Figure 7(a). After that (see Figure 5(d) and the associated animation), the reconnected inner peripheral loops drastically erupt outward; the outer ones expand significantly, which may be resulted from enhanced magnetic pressure higher up by the lateral expansion of erupting structures; and the ones in between sequentially contract into the magnetic-energy-releasing core. The drastic increase in plasma kinetic energy after around $t = 9$ can also be seen later in Figure 7(a). Thus the expansion and contraction of the peripheral loops are well correlated with the accumulation and dissipation of magnetic energy in the central region.

We then focus on the representative dynamics of L11 in Figures 6. Because the Alfvén frozen flux theorem applies in the coronal MHD environment (Priest 2014), the magnetic field changes as if it moves with the plasma, thus when we trace the magnetic loop, the material derivative in the momentum Equation (2) is considered for the plasma dynamics. On the right hand side of the momentum Equation (2), Lorentz force dominates in the low- β coronal condition. Lorentz force can be decomposed into two components, inward magnetic tension force and outward magnetic pressure gradient force, while the parallel components to the magnetic field line of these two forces cancel with each other (Priest 2014), we thus only pay attention to their normal components to the magnetic field line, abbreviated as MTN and MPN hereafter. In Figures 6 we have them plotted for L11 colored by their magnitudes using the same colorbar (F/ρ represents MTN or MPN weighted by density). At $t = 0$ (Figure 6(a)), MTN and MPN are well balanced. Then MPN increases to be larger than MTN as L11 expands (Figure 6(b)). At $t = 10$ (Figure 6(c)), they both reduce significantly but MTN starts to be larger than MPN until the end of the simulation (Figure 6(d)), which results in the considerable contraction of L11.

To be more specific and quantitative, we select the midpoint of L11 to investigate the evolution of MTN and MPN on it. The evolutions of normalized values of L11 distance as in Figure 3(b), magnetic energy E_m and plasma kinetic energy E_k in the simulation volume are added in Figure 7(a) for reference. Together with MTN and MPN, magnetic energy density represented by B^2 and curvature radius calculated as $R_c = B^2/\text{MTN}$ (Priest 2014) at the midpoint of L11 are also illustrated in Figure 7(b). MTN, MPN, and B^2 are all weighted by density ρ , which can be considered as the quantities averaged on each particle. We note that magnetic tension force and magnetic pressure gradient force are not necessarily antiparallel with each other, also for their components, MTN and MPN, which is not considered in Zuccarello et al. (2017). Thus it is indispensable to take the angle between MTN and MPN into account for further discussion, as shown in Figure 7(c). The data for the angle are also colored red or blue, representing the Lorentz force in z direction (or the z component of the net force of MTN and MPN > 0 or < 0 , indicating upward or downward acceleration. The dashed line in each figure denotes the inflection point from expansion to contraction for L11. First, combining Figure 7(a) and Figure 7(c), we can separate the motion of L11 into 4 quadrants. For example, from $t = 0$ to around $t = 4$, L11 expands (Figure 7(a)) and also is accelerated upwards (Figure 7(c)), thus categorized as quadrant 1, while in quadrant 2 L11 is accelerated downward as expanding. Quadrants 3 and 4 are also deduced in the same way. This evolution of motion of L11 is just a vortex flow proposed by Zuccarello et al. (2017), which can also be seen later in Figure 8(a).

Figures 7(b) and (c) show that at $t = 0$ MTN and MPN balance well with their magnitudes close and angle antiparallel, as mentioned earlier for Figure 5(e). Then significant enhancement of MPN over MTN until $t = 7$ causes L11 to be pushed outward by the expanding reconnected structure in the center. Meanwhile, as the central reconnected structure inflates continuously, the direction of MPN changes from upward and outward to downward and outward, which makes the decrease in the angle between MTN and MPN, and the transition from upward to downward of the z component of the total Lorentz force. This is consistent with the motion of L11 from quadrant 1 to quadrant 2 in the vortex flow. During this period, MTN changes little because B^2 increases almost in proportion to R_c . Though the magnetic energy in the whole simulation volume decreases from $t = 0$ to $t = 7$ (Figures 7(a)), it does not make the outward MPN on L11 decrease because the green magnetic energy profile inflates while the magnetic energy dissipation mainly occurs in the very center associated with the central tether-cutting reconnection, as can be seen from Figure 5(e) to Figure 5(f). At around $t = 8$, both MTN and MPN begin to reduce, and the reductions become significant at around $t = 9$, which we

suppose is induced by the runaway magnetic energy dissipation in the central tether-cutting reconnection as presented in Figure 5(c) and Figures 7(a). The drastic eruption then follows as seen from the kinetic energy evolution in Figures 7(a) (also from Figure 5 and the associated animations). MTN can be reduced because after around $t = 8 R_c$ grows faster while B^2 begins to decrease. This conforms to physical intuition since the central magnetic liberation could make it easier for peripheral loops to become straight and relaxed. The more drastic reduction in MPN than in MTN leads to the total Lorentz force starting to be inward and downward at around $t = 10$, thus generating the contraction motion of L11 in quadrant 3 of the vortex flow, which is contrary to the suggestion by Zuccarello et al. (2017) that the enhancement of MTN in excess of MPN in the expansion phase finally causes the loop to contract. The analysis supports the idea that it is the reduction of magnetic energy of the core region which reduces the outward magnetic pressure resulting in the contraction of peripheral magnetic loops conjectured by Hudson (2000). As can be imagined, when the reconnected core structure erupts away, the downward component of MPN is also reduced, thus making the angle between MTN and MPN continuously recovered in quadrant 3.

At around $t = 15$, L11 steps into quadrant 4 of the vortex flow. Though at this moment the magnitudes of MTN and MPN become stable, the direction of MPN begins to incline upward and inward as checked in the data, which results in the decrease in the angle between MTN and MPN again and the total Lorentz force pointing upward and inward. This is because that there is a strong attraction from a current sheet of low magnetic pressure created by the reconnection between the peripheral contracting and the central erupting structures, which will be discussed in the next section.

3.3. Reconnection between Contracting and Erupting Structures

Figure 8(a) shows the reconnection between the peripheral contracting magnetic loops (yellow field lines) and the central erupting magnetic structures (blue field lines). They act as inflows into a current sheet created between them. It has also been pointed out, **in our discussion of Figures 4(a) and (b) in Section 3.1**, that the shrinking loops can be a second inflow in addition to the traditional central inflow. Red field lines are the reconnection upflow, and green ones the reconnection downflow. We can see this scenario more clearly in 3D in Figure 8(b). Because of the reconnection the identity of the original contracting loops would disappear. It thus could be one possible explanation for the disappearance of the shrinking loops in the late phase of contraction from all AIA wavebands in observations.

It is shown in Figure 8(c) that the reconnected peripheral loops (red field lines) pass through part of the lobe of the Ω

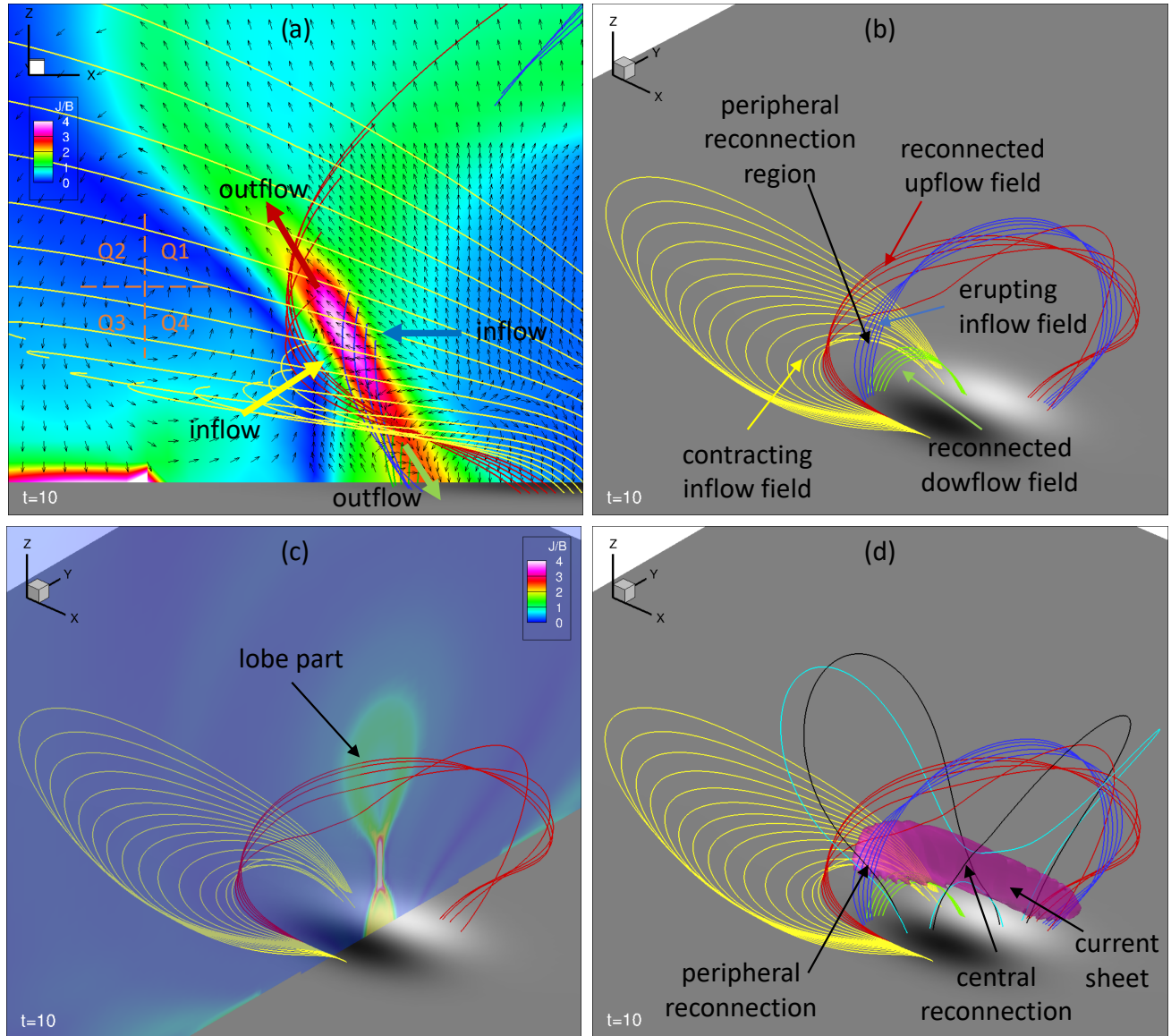


Figure 8. The reconnection between contracting and erupting fields in the periphery. (a) vortex flow associated with the selected magnetic loops in Figure 2, and the peripheral reconnection scenario. The chosen slice is the $y = -1$ plane, colored by weighted current density and also added with arrows indicating velocity vectors in the plane. Q_n ($n = 1, 2, 3, 4$) separated by the two dashed line dividing sections of the vortex flow represents quadrant n in Figure 7(c) for simplicity. (b) The peripheral reconnection scenario in 3D. (c) shows that the reconnected outflowing field lines (red) penetrate through the lobe part of the Ω structure of high current density in the $x = 0$ plane. (d) the relative position of the asymmetric peripheral reconnection to the symmetric central tether-cutting reconnection. The magenta isosurface denotes the current sheet profile of $J/B = 3.2$. The animated version of (d) in 3D view is available.

structure of high current density, different from the standard “CSHKP” flare model where the upflowing structure reconnected from the central current sheet constitutes the lobe part. We also note in Figure 5(d) that the reconnected peripheral loops are anchored at the hook part of the J-shaped ribbon, consistent with the discovery of [Aulanier & Dudík \(2019\)](#). Figure 8(d) and the animation attached show the relative position of the peripheral reconnection to the central one. It can be seen that the peripheral reconnection is a product of the transition of the reconnection structure along the current

sheet (magenta isosurface) from symmetric in the center towards asymmetric at the periphery; and it is just located at the elbow extension part of the inverse S shaped current sheet.

4. DISCUSSION AND CONCLUSIONS

We have exploited a 3D, fully MHD simulation to study peripheral loop contraction and disappearance in solar events. The inner ones of the selected magnetic loops at the periphery are found to slip into the central magnetic energy liberation region and to reconnect forming a sigmoid

structure. This behavior has not been observed in previous implosion studies since these inner structures are sometimes invisible by the instruments used (e.g., Wang et al. 2016) or too close to the flaring core (e.g., Simões et al. 2013). The middle and outer loops selected expand and then contract in sequence from inner to outer towards the central erupting region, substantiating the reality of the contraction motion rather than just being a projection effect of inclination. The transition from expansion to contraction for some peripheral loops in the simulation is consistent with several events (Wang et al. 2016, 2018), though it is also found in observation that large scale loops can directly contract without the expansion phase at first (Gosain 2012; Liu et al. 2012; Sun et al. 2012; Simões et al. 2013; Yan et al. 2013; Kushwaha et al. 2015; Petrie 2016; Wang et al. 2018).

From either graphical in Figure 8(a) or quantitative inspection in Figure 7(c), the contraction following expansion of the peripheral loops constitutes a vortex flow of four quadrants, which is consistent with the discovery in Zuccarello et al. (2017) and Dudík et al. (2017). However, the physical cause of the loop shrinkage is found to be different from their proposal introduced in Section 1. First, the loop motion at the periphery correlates well with magnetic energy release in the center, and controlled by its induced changes in two Lorentz force components, as illustrated in Figure 5. Then through detailed analysis in Figure 7 of the changes in physical quantities, MTN, MPN, B^2 , R_c , and the angle between MTN and MPN, we conclude that it is the drastic reduction in MPN by the accelerated central magnetic energy dissipation that causes the peripheral loop to reverse motion to contract, in support of the conjecture by Hudson (2000). In contrast to the prediction in Zuccarello et al. (2017), the magnetic tension force MTN enhances little during the loop expansion, because B^2 varies almost in proportion to the curvature radius R_c . MTN is also found to be reduced as the central magnetic energy dissipation rapidly intensifies because with less press from the center, magnetic loops tend to become straight and relaxed, conforming to physical intuition, but the much more decrease in MPN than in MTN finally leads to the contraction of magnetic loops in the periphery.

When the peripheral loops continue to contract and enter into quadrant 4 of the vortex flow, they move inward and upward to reconnect with the central erupting structures, which is the reason they behave as a second inflow embedded between two current sheets. The reconnection would destroy the original identities of the shrinking loops, which thus naturally provides a possible explanation for their disappearance observed at the periphery in the late phase (Liu & Wang 2009; Sun et al. 2012; Simões et al. 2013; Yan et al. 2013; Kushwaha et al. 2015; Petrie 2016; Wang et al. 2016, 2018). It should be noted that other possibilities, like plasma draining, cooling or heating, could still remain in different situa-

tions, which needs further investigations including both simulations and observations.

The peripheral reconnection has also been discovered by Aulanier & Dudík (2019) in simulation recently, and verified by following observations (Zemanová et al. 2019; Lörinčík et al. 2019; Dudík et al. 2019). It is referred to as “ar-rf reconnection” by the authors, where “a” denotes arcade, “r” flux rope, and “f” flare loop. This kind of reconnection occurring at the periphery is an attribute of 3D reconnection geometry, which can result in drifting of erupting flux rope footpoints. Our work shows that the involved arcade in the “ar-rf reconnection” could be the contracting loops in the returning part of the vortex flow created at the periphery.

In this simulation, the peripheral reconnection, located at the elbow of the inverse S shaped current sheet, is the asymmetric extension of the symmetric tether-cutting reconnection at the center. The inflow field from the erupting structure (blue field lines in Figure 8(d)) for the peripheral reconnection is situated above both the central current sheet and the concave-upward part of the long loop (long cyan field line) emanating from the central reconnection, thus it behaves as constraint for underlying central eruption. As we can imagine, continuous peripheral reconnection (between yellow and blue field lines) can make this constraining field to expand as outflows due to outward enhanced tension of newly reconnected field lines, which then facilitates the eruption of the central structure underneath. The central eruption can promote the vortex flow for the contracting inflow field to be reconnected in the periphery. Accordingly, the peripheral reconnection and the eruption of the reconnected core structure form a positive feedback. In term of results, this is similar to the often quoted positive feedback created between eruption and central reconnection.

We have to note that the results here are limited to the simulation and the specified model settings. It is encouraged to use various numerical methods and configurations to test the conclusions. Further observations about peripheral implosions will hopefully provide more actual information.

ACKNOWLEDGMENTS

J. W. acknowledges support from the International Postdoctoral Exchange Fellowship Program, Guangdong Basic and Applied Basic Research Foundation (2019A1515111008), China Postdoctoral Science Foundation (2020M670897), National Natural Science Foundation of China (NSFC 12003005). C. J. acknowledges support from National Natural Science Foundation of China (NSFC 41822404, 41731067), the Fundamental Research Funds for the Central Universities (Grant No.HIT.BRETIV.201901), and Shenzhen Technology Project (JCYJ20190806142609035).

REFERENCES

- Aly, J. J. 1984, *ApJ*, 283, 349, doi: [10.1086/162313](https://doi.org/10.1086/162313)
- . 1991, *ApJL*, 375, L61, doi: [10.1086/186088](https://doi.org/10.1086/186088)
- Amari, T., Luciani, J. F., Aly, J. J., Mikić, Z., & Linker, J. 2003, *ApJ*, 585, 1073, doi: [10.1086/345501](https://doi.org/10.1086/345501)
- Aulanier, G., Démoulin, P., & Grappin, R. 2005, *A&A*, 430, 1067, doi: [10.1051/0004-6361:20041519](https://doi.org/10.1051/0004-6361:20041519)
- Aulanier, G., & Dudík, J. 2019, *A&A*, 621, A72, doi: [10.1051/0004-6361/201834221](https://doi.org/10.1051/0004-6361/201834221)
- Aulanier, G., Török, T., Démoulin, P., & DeLuca, E. E. 2010, *ApJ*, 708, 314, doi: [10.1088/0004-637X/708/1/314](https://doi.org/10.1088/0004-637X/708/1/314)
- Dudík, J., Lörinčík, J., Aulanier, G., Zemanová, A., & Schmieder, B. 2019, *ApJ*, 887, 71, doi: [10.3847/1538-4357/ab4f86](https://doi.org/10.3847/1538-4357/ab4f86)
- Dudík, J., Zuccarello, F. P., Aulanier, G., Schmieder, B., & Démoulin, P. 2017, *ApJ*, 844, 54, doi: [10.3847/1538-4357/aa7aab](https://doi.org/10.3847/1538-4357/aa7aab)
- Fan, Y. 2010, *ApJ*, 719, 728, doi: [10.1088/0004-637X/719/1/728](https://doi.org/10.1088/0004-637X/719/1/728)
- Fan, Y., & Gibson, S. E. 2007, *ApJ*, 668, 1232, doi: [10.1086/521335](https://doi.org/10.1086/521335)
- Gibson, S. E., & Fan, Y. 2006, *Journal of Geophysical Research (Space Physics)*, 111, A12103, doi: [10.1029/2006JA011871](https://doi.org/10.1029/2006JA011871)
- Gosain, S. 2012, *ApJ*, 749, 85, doi: [10.1088/0004-637X/749/1/85](https://doi.org/10.1088/0004-637X/749/1/85)
- Hudson, H. S. 2000, *ApJL*, 531, L75, doi: [10.1086/312516](https://doi.org/10.1086/312516)
- Jiang, C., Feng, X., Zhang, J., & Zhong, D. 2010, *SoPh*, 267, 463, doi: [10.1007/s11207-010-9649-6](https://doi.org/10.1007/s11207-010-9649-6)
- Kushwaha, U., Joshi, B., Veronig, A. M., & Moon, Y.-J. 2015, *ApJ*, 807, 101, doi: [10.1088/0004-637X/807/1/101](https://doi.org/10.1088/0004-637X/807/1/101)
- Linker, J. A., Mikić, Z., Lionello, R., et al. 2003, *Physics of Plasmas*, 10, 1971, doi: [10.1063/1.1563668](https://doi.org/10.1063/1.1563668)
- Liu, R., Liu, C., Török, T., Wang, Y., & Wang, H. 2012, *ApJ*, 757, 150, doi: [10.1088/0004-637X/757/2/150](https://doi.org/10.1088/0004-637X/757/2/150)
- Liu, R., & Wang, H. 2009, *ApJL*, 703, L23, doi: [10.1088/0004-637X/703/1/L23](https://doi.org/10.1088/0004-637X/703/1/L23)
- . 2010, *ApJL*, 714, L41, doi: [10.1088/2041-8205/714/1/L41](https://doi.org/10.1088/2041-8205/714/1/L41)
- Lörinčík, J., Dudík, J., & Aulanier, G. 2019, *ApJ*, 885, 83, doi: [10.3847/1538-4357/ab4519](https://doi.org/10.3847/1538-4357/ab4519)
- Pascoe, D. J., Russell, A. J. B., Anfinogentov, S. A., et al. 2017, *A&A*, 607, A8, doi: [10.1051/0004-6361/201730915](https://doi.org/10.1051/0004-6361/201730915)
- Petrie, G. J. D. 2016, *SoPh*, 291, 791, doi: [10.1007/s11207-016-0873-6](https://doi.org/10.1007/s11207-016-0873-6)
- Priest, E. 2014, *Magnetohydrodynamics of the Sun*, Springer Netherlands
- Rachmeler, L. A., DeForest, C. E., & Kankelborg, C. C. 2009, *ApJ*, 693, 1431, doi: [10.1088/0004-637X/693/2/1431](https://doi.org/10.1088/0004-637X/693/2/1431)
- Russell, A. J. B., Simões, P. J. A., & Fletcher, L. 2015, *A&A*, 581, A8, doi: [10.1051/0004-6361/201525746](https://doi.org/10.1051/0004-6361/201525746)
- Sarkar, A., Vaidya, B., Hazra, S., & Bhattacharyya, J. 2017, *ApJ*, 851, 120, doi: [10.3847/1538-4357/aa9a45](https://doi.org/10.3847/1538-4357/aa9a45)
- Simões, P. J. A., Fletcher, L., Hudson, H. S., & Russell, A. J. B. 2013, *ApJ*, 777, 152, doi: [10.1088/0004-637X/777/2/152](https://doi.org/10.1088/0004-637X/777/2/152)
- Sturrock, P. A. 1991, *ApJ*, 380, 655, doi: [10.1086/170620](https://doi.org/10.1086/170620)
- Sturrock, P. A., Weber, M., Wheatland, M. S., & Wolfson, R. 2001, *ApJ*, 548, 492, doi: [10.1086/318671](https://doi.org/10.1086/318671)
- Sun, J. Q., Cheng, X., Ding, M. D., et al. 2015, *Nature Communications*, 6, 7598, doi: [10.1038/ncomms8598](https://doi.org/10.1038/ncomms8598)
- Sun, X., Hoeksema, J. T., Liu, Y., et al. 2012, *ApJ*, 748, 77, doi: [10.1088/0004-637X/748/2/77](https://doi.org/10.1088/0004-637X/748/2/77)
- Török, T., Downs, C., Linker, J. A., et al. 2018, *ApJ*, 856, 75, doi: [10.3847/1538-4357/aab36d](https://doi.org/10.3847/1538-4357/aab36d)
- Wang, J., Simões, P. J. A., & Fletcher, L. 2018, *ApJ*, 859, 25, doi: [10.3847/1538-4357/aabc0e](https://doi.org/10.3847/1538-4357/aabc0e)
- Wang, J., Simões, P. J. A., Fletcher, L., et al. 2016, *ApJ*, 833, 221, doi: [10.3847/1538-4357/833/2/221](https://doi.org/10.3847/1538-4357/833/2/221)
- Yan, X. L., Pan, G. M., Liu, J. H., et al. 2013, *AJ*, 145, 153, doi: [10.1088/0004-6256/145/6/153](https://doi.org/10.1088/0004-6256/145/6/153)
- Zemanová, A., Dudík, J., Aulanier, G., Thalmann, J. K., & Gömöry, P. 2019, *ApJ*, 883, 96, doi: [10.3847/1538-4357/ab3926](https://doi.org/10.3847/1538-4357/ab3926)
- Zou, P., Jiang, C., Wei, F., Zuo, P., & Wang, Y. 2019, *ApJ*, 884, 157, doi: [10.3847/1538-4357/ab4355](https://doi.org/10.3847/1538-4357/ab4355)
- Zuccarello, F. P., Aulanier, G., Dudík, J., et al. 2017, *ApJ*, 837, 115, doi: [10.3847/1538-4357/aa6110](https://doi.org/10.3847/1538-4357/aa6110)